

Sleeve Slippage Simulation and Slippage Damage Identification for the Development of Next Generation Sleeve Assembly Roll

Nao-Aki Noda^{1,a*}

¹Kyushu Institute of Technology, Kitakyushu 804-8550, Japan

^anao592noda@gmail.com, *Corresponding author

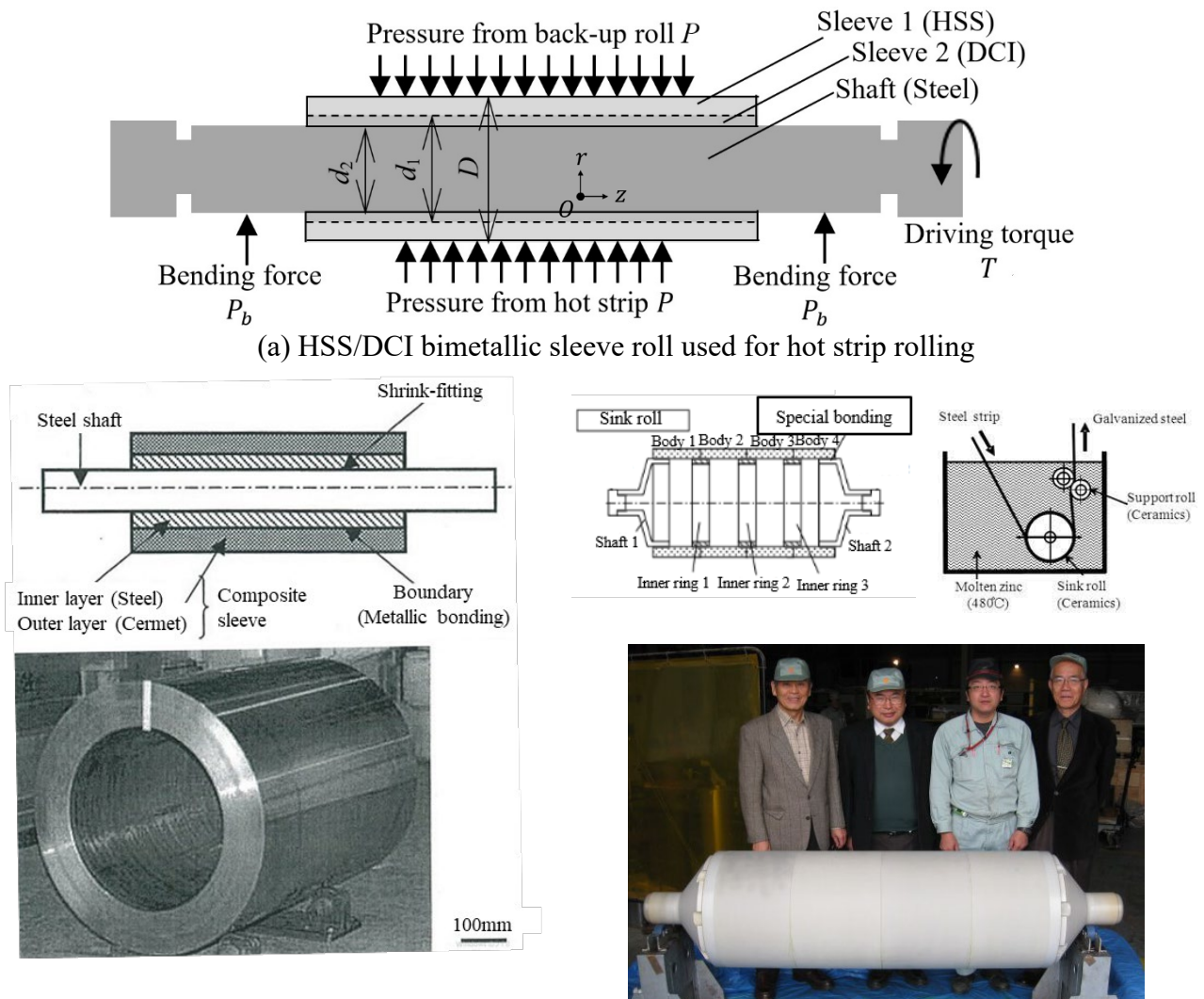
Keywords: Work roll, Fatigue strength, Sleeve roll, Residual Stress, Sleeve slippage, Slippage damage, Rolling, Load shifting method, Miniature roll experiment

Abstract. Next generation rolls such as super-cermet rolls and all-ceramic rolls can be manufactured using only sleeve assembly type rolls, which have the advantage of being able to reuse the shaft by replacing the damaged sleeves. However, in some cases, failures with unknown causes may occur such as circumferential slippage, shaft pull-out or residual bending deformation at the shrink-fit interface. Such slipping failures cannot be prevented by conventional design concept. This is because even if the resistant torque is greater than the motor torque, the circumferential slippage will occur. Through numerical simulation and miniature roll experiment, the following results are obtained. 1) Even under free rolling condition without motor torque, the circumferential slippage occurs. 2) The slippage is caused by the accumulation of irreversible slip during the roll rotation. 3) The motor torque accelerates the slip amount significantly. 4) The geometry of slippage defect can be identified experimentally. 5) The fatigue strength of sleeve assembly rolling rolls can be evaluated by using \sqrt{area} parameter characterizing the identified slip defects. 6) By preventing the slip damage, the fatigue strength of sleeve rolls can be nearly equal to that of conventional solid rolls without shrink-fit.

1. Introduction

In metalworking, rolling processes more tonnage than any other manufacturing process. Rolling technology is developing and advancing further although seemingly mature. The rolling rolls are classified into two types; one is a single-solid type mainly used, and the other is a shrink-fitted assembled type consisting of a sleeve and a shaft. Several sleeve assembly types are being successfully used by shrink-fitting a shaft into a hollow cylinder [1-8]. Previously, Shimoda et al [1] and Tutumi et al [7] discussed residual deformations of sleeve rolls. Irie et al [2] and Takigawa et al explained new technology in rolling. Sano summarized recent advances in rolling roll [4-6]. As described in those references, the sleeve rolls have the following advantages. 1) The shaft can be reused by replacing the sleeve after consumed due to the abrasion or the surface roughening. 2) The sleeve wear resistance can be improved independently without loosening the shaft ductility. 3) Next generation rolls such as the super-cermet roll [9] and all ceramic roll [10-12] can be manufactured only as a sleeve roll as described in Hamayoshi et al [10] and Noda et al [11, 12].

Fig. 1 (a) illustrates a bimetallic sleeve roll used for hot strip rolling. The HSS/DCI sleeve is manufactured by centrifugal casting method and shrink-fitted to the steel shaft. Here, the two-layer sleeve consists of the outer layer which is made of high-speed steel (HSS) having both wear resistance and toughness, and the inner layer is made of ductile casting iron (DCI) having high ductility. Fig. 1 (b) illustrate a super-cermet composite sleeve roll used for hot strip rolling as a next generation roll [9]. Fig. 1 (c) illustrate an all-ceramic sleeve roll used for used for molten zinc bath in continuous galvanizing line as the next generation roll [10-12].



(b) Super-cermet composite sleeve roll used for hot strip rolling

(c) All ceramic sleeve roll used for molten zinc/aluminium bath in continuous galvanizing line

Fig.1 Some sleeve roll example

To develop those shrink-fitted sleeve roll, several peculiar problems such as circumferential slip must be solved. In the authors' previous studies, numerical simulations and experiments were conducted to clarify these phenomena. This review paper summarizes the authors' recent consecutive work on the new failure of sleeve slippage appearing in sleeve rolls [13-15, 29-31] in the following way.

- Section 2 shows the load shifting simulation method to realize this unknown slip failure [13, 14] indicating that even under free rolling without motor torque, the circumferential slippage occurs.
- Section 3 clarifies the effects of motor torque on the slip amount.
- Section 4 describes that the miniature roll experiments confirm the simulation's validity [15, 29-31].
- Section 5 explains three-dimensional defect geometry appearing during the roll rotation[30].
- Section 6 discusses the fatigue strength of sleeve rolls based on the simulation and defect dimensions identified[31].

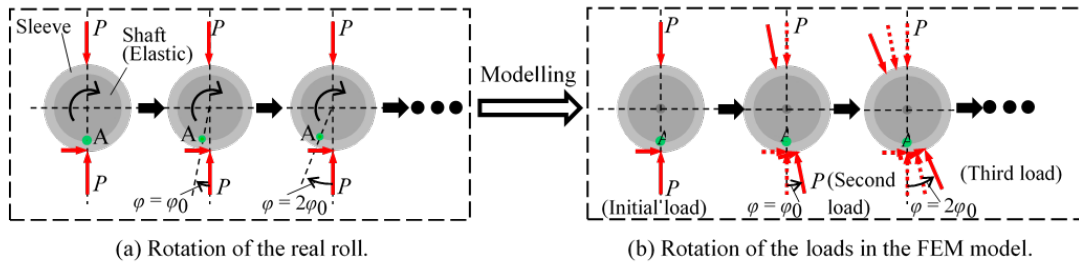
2. Unknow Sleeve Slippage and Proposed Simulation Method to Clarify THIS Failure

Among peculiar problems of sleeve rolls, no detail studies are available for circumferential slippage. The circumferential slippage sometimes occurs even though the resistance torque at the interface is larger than the motor torque. Similar phenomenon is known as "interfacial creep" in ball bearing. In this failure, the bearing gradually moves circumferentially to the stationary shaft or housing [15-26].

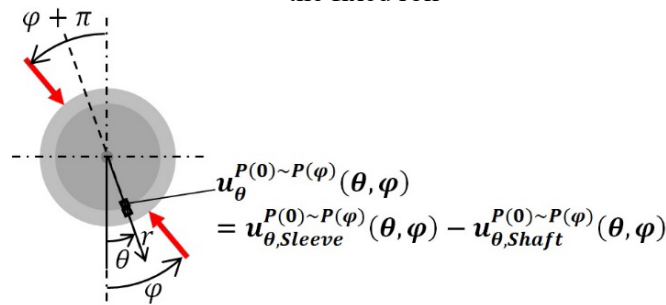
To explain this failure, Soda [16] explained two factors; one is the clearance between the ring and the shaft or housing, and the other is the elastic deformation which Imai [17] proved experimentally. Those studies treated the interface creep in the opposite direction to the bearing rotation [17, 18] but other reports treated the creep in the same direction [19, 20]. Several other studies are also available for the bearing creep phenomenon [21-28]. However, few studies discussed the phenomenon quantitatively.

Fig.2 illustrates the load shifting method proposed to clarify this unknown failure. Here, the roll rotation is expressed by shifting the load on the fixed roll surface [11-15, 29-31]. Assume the work roll is subjected to the concentrated rolling load P . As shown in Fig. 2, the continuous roll rotation can be expressed by the discrete load shifting with a constant interval φ_0 . The most suitable value of φ_0 can be chosen to reduce the computational time without loosening the accuracy. Then, in the previous studies [13-15], the amount of the slip was investigated by varying several design factors such as shaft deformation, motor torque and shrink-fitting ratio. Since the displacement $u_{\theta}^{P(0)\sim P(\varphi)}(\theta)$ varies depending on θ , the average displacement can be defined in Eq.(1)[11-15, 29-31].

$$u_{\theta,ave.}^{P(0)\sim P(\varphi)} = \frac{1}{2\pi} \int_0^{2\pi} u_{\theta}^{P(0)\sim P(\varphi)}(\theta) d\theta \quad (1)$$



(a) Load shifting method where the roll rotation is replaced by discrete load shifting by the angle φ_0 on the fixed roll



$$u_{\theta,ave.,T=T_m}^{P(0)\sim P(\varphi)}(\varphi) = \frac{1}{2\pi} \int_0^{2\pi} u_{\theta}^{P(0)\sim P(\varphi)}(\theta, \varphi) d\theta$$

(b) Definition of interfacial displacement $u_{\theta}^{P(0)\sim P(\varphi)}(\theta, \varphi)$ due to the load shifting $P(0)\sim P(\varphi)$ and the average displacement $u_{\theta,ave.,T=T_m}^{P(0)\sim P(\varphi)}(\varphi)$ to express the amount of the slip with increasing φ .

Fig. 2. Illustration for load shifting simulation method to realize the interface slip

Fig. 3 illustrates two-dimensional modelling in numerical simulation when the sleeve consists of high-speed material and ductile material with steel shaft. By applying the load shifting method [13-15, 29-31], the roll rotation is expressed by the load shifting on the fixed roll surface. Fig. 3(a) illustrates the real roll expressed by shifting the load on the roll surface with the roll center fixed. The roll is assumed to be subjected to the concentrated rolling load P . In rolling the friction S is used to compress the rolling plate between the rolls as well as the driving torque T from the motor to the shaft. Fig.3 (b) shows the model for numerical simulation by putting a rigid body at the center to restrain the displacement and rotation of the center of the roll. It is confirmed that the rigid body size at the center does not affect the result, and the diameter 8 mm is used. Fig. 3(b) also shows an example of the mesh division for the finite element method (FEM).

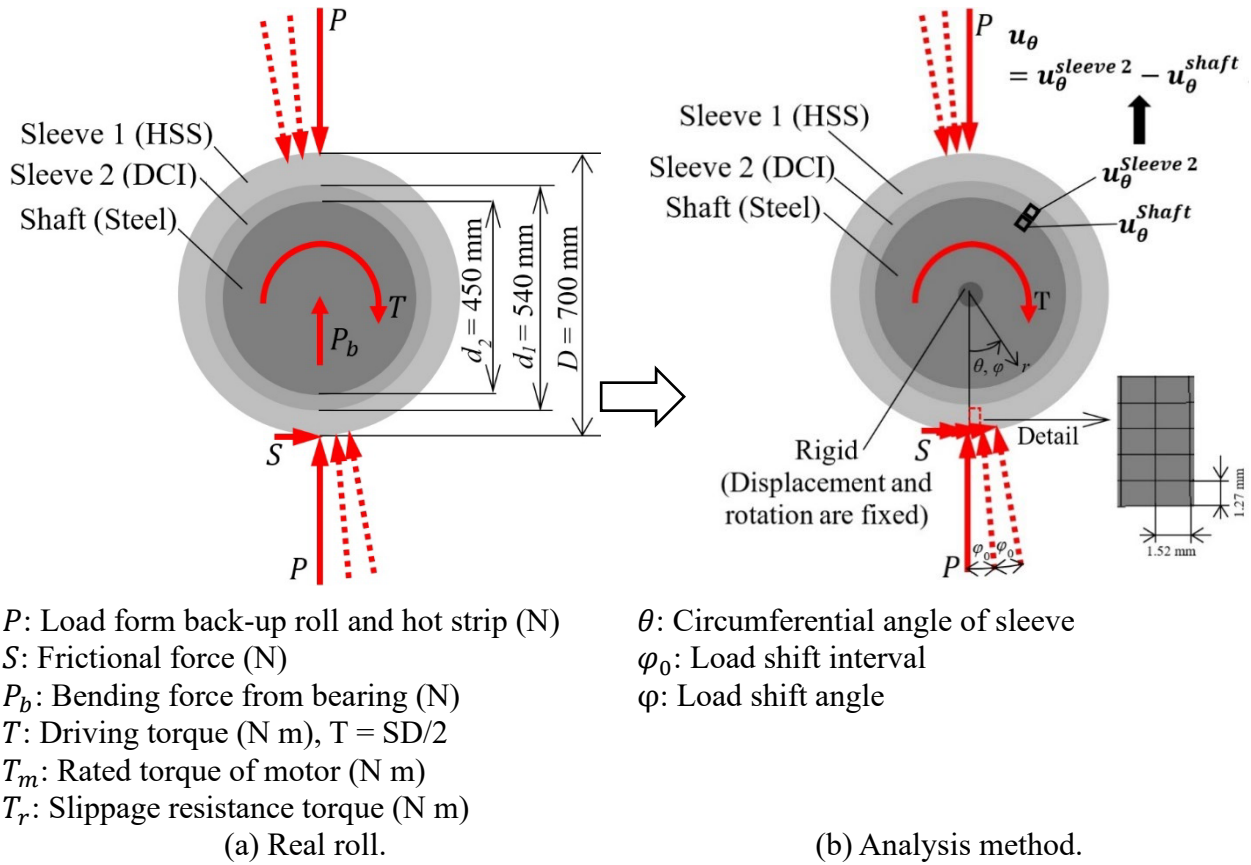


Fig. 3. Modelling for bimetric sleeve roll.

The Finite Element Method (hereinafter abbreviated as FEM) is used for the numerical analysis of the sleeve assembly type roll in Fig. 2. To realize the interface slippage, the FEM simulation should be well conducted on basis of the experience and skills for engineering. Then, the circumferential sleeve slippage will be realized by extending the above technique and applying FEM code Marc/Mentat 2012 to the elastic contact quasi-static analysis for rolling rolls. In this code, the complete Newton-Raphson method and the direct constraint method for the contact analysis are used. As shown in Fig. 2(b), a 4-node quadrilateral plane strain is used with the number of mesh elements are $6. \times 10^5$ with confirming the mesh independency of the results.

Table 1 shows the work roll's dimensions, mechanical properties, and boundary conditions used in the analysis. In this study, the standard compressive force P is $P = P_0$ and the standard drive torque is $T = T_m$. The loading condition used in this study is based on the data at No. 5 stand for roll hot strip finishing roll mill [4, 5]. Assume conditions equivalent to hot rolling of ordinary steel sheets, a standard load $P = P_0 = 13270$ N/mm per 1 mm of roll is used. Small effect can be confirmed by replacing Hertzian contact stress with the concentrated force P . Instead of the standard force $P = P_0$ with the standard drive torque $T = T_m$, this study focuses on the rolling load $P = 1.5P_0$ with the drive torque $T = 1.5T_m$, which is corresponding to the impact load when the rolled plate biting trouble occurs. The shrink-fitting ratio is defined as δ/d , where δ is the diameter difference between the inner diameter of the sleeve and the outer diameter of the shaft. Usually, the shrink-fitting ratio in the range $\delta/d = 0.4 \times 10^{-3} \sim 1.0 \times 10^{-3}$ is applied to sleeve rolls on the basis of long year experience. To study the irreversible interfacial slip, in this paper, $\delta/d = 0.5 \times 10^{-3}$ is focused. The effect of the shrink-fitting ratio has been discussed [11-15, 29, 30]. Regarding the friction coefficient μ controlling the slippage resistance on the interface, $\mu = 0.2$ was used in an experimental study and $\mu = 0.4$ was often used for steel surfaces previously [1, 15, 29-31]. In this way, since $\mu = 0.2 \sim 0.4$ is usually used for sleeve assembly type rolls, in this study, the friction coefficient $\mu = 0.3$ between the sleeve and the shaft is used.

Table 1. Dimensions, mechanical properties and boundary conditions in Figure 1 considered as a standard roll in this study.

Mechanical properties	Sleeve	Shell	E_{sleeve}	233 GPa
			ν_{sleeve}	0.3
		Core	E_{sleeve}	173 GPa
			ν_{sleeve}	0.3
	Shaft		E_{shaft}	210 GPa
			ν_{shaft}	0.28
Roll size		Outer diameter of sleeve D		700 mm
		Inner diameter sleeve d_1		540 mm
		Inner diameter sleeve d_2		450 mm
Shrink fitting		Shrink fitting ratio δ/d		0.5×10^{-3}
		Friction coefficient between sleeve and shaft μ		0.3
External force		Concentrated load per unit width $P = P_0$		13270 N/mm
		Frictional force per unit width S		Total: 1.327×10^7 N
		Motor torque per unit width T_m		Rolled width: 1000 mm
		Resistance torque per unit width T_r		1346 N/mm
		Bending force from bearing P_b		471 Nm/mm
				3193 Nm/mm
				0 N/mm

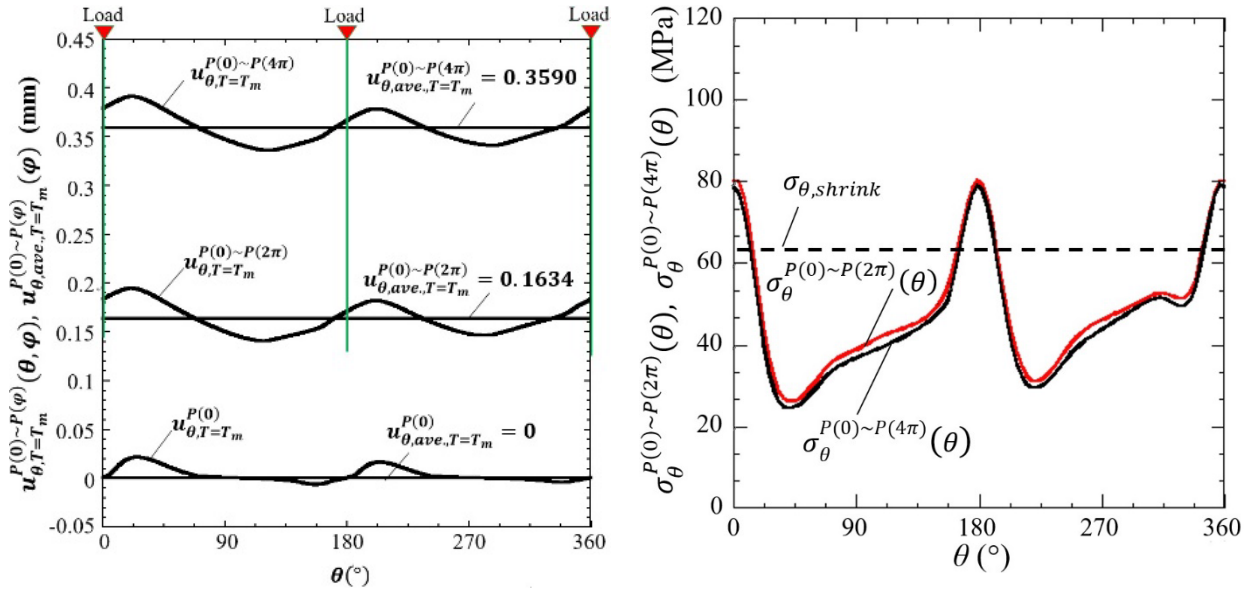
3. Results and Discussion: Irreversible Slip Accumulation for Interfacial Displacement and Non-Accumulation of Rolling Stress σ_θ

In the sleeve roll, the circumferential slippage sometimes occurs even though the resistance torque at the interface is larger than the motor torque. In the previous studies, the interfacial slip was realized by the load shifting method [13-15, 29-31]. Fig. 4 (a) illustrates the interfacial slip $u_\theta^{P(0)}(\theta)$, which is the relative displacement u_θ at $\theta = \theta$ when the initial load $P = P_0$ is applied at $\varphi = 0$ as $P(0)$. Fig. 4 (a) also shows $u_\theta^{P(0) \sim P(2\pi)}(\theta)$, which is the circumferential displacement u_θ when the load $P = P_0$ moves from $\varphi = 0$ to $\varphi = 2\pi$ as $P(0) \sim P(2\pi)$. Fig. 4(a) also shows $u_\theta^{P(0) \sim P(4\pi)}(\theta)$ when the load $P = P_0$ moves two rotations as $P(0) \sim P(4\pi)$. As shown in Fig. 4(a), the displacement $u_\theta^{P(0) \sim P(\varphi)}(\theta)$ increases with increasing φ . As shown in Fig.4 (a), it can be seen more clearly that the average displacement $u_{\theta,ave}^{P(0) \sim P(\varphi)} = \frac{1}{2\pi} \int_0^{2\pi} u_\theta^{P(0) \sim P(\varphi)}(\theta) d\theta$ increases due to the load shifting from $\varphi = 0$ to $\varphi = 4\pi$.

If such circumferential slip $u_\theta^{P(0) \sim P(\varphi)}(\theta)$ occurs in a real rolling roll, several scratches and partial seizure happen at the sleeve shrink-fitting surface. Then, the seizure growth with the roll rotation causes the surface roughness with a few millimeters' depth. Due to the roughness, fatigue crack initiates and propagates at the sleeve inner surface causing the final fracture [6]. Considering such failure, the stress σ_θ at the shrink-fitted surface is focused in this paper since σ_θ is the largest stress component and causes such damage. The stress $\sigma_\theta^{P(0) \sim P(\varphi)}(\theta)$ is defined as the interface stress σ_θ due to the load shifting $P(0) \sim P(\varphi)$ when the load moves from the angle $\varphi = 0$ to $\varphi = \varphi$. Here, notation φ denotes the angle where the load is shifting and notation θ denotes the position where the stress is considered. The load $P(\varphi)$ is defined as the pair of forces acting at $\varphi = \varphi$ and $\varphi = \varphi + \pi$. The notation $\sigma_\theta^{P(0) \sim P(\varphi)}(\theta)$ means the stress $\sigma_\theta(\theta)$ at $\theta = \theta$ when the pair of loads are applied at $\varphi = 0$ to $\varphi = \varphi$ and $\varphi = \pi$ to $\varphi = \varphi + \pi$.

Fig. 4 (b) shows the stress distribution, $\sigma_\theta^{P(0) \sim P(2\pi)}(\theta)$, which is the stress σ_θ when the load $P = P_0$ moves one rotation as $P(0) \sim P(2\pi)$. Fig. 4(b) also shows $\sigma_\theta^{P(0) \sim P(4\pi)}(\theta)$ when the load $P = P_0$ moves two rotations as $P(0) \sim P(4\pi)$. As shown in Fig. 3(b), no large difference between σ_θ after one rotation and σ_θ after two rotations of the load P . In other words, the accumulation phenomenon observed in the displacement is not seen in the stress. For the fatigue risk evaluation, therefore, the

stress obtained by after two rotations can be always used irrespective of the number of the roll rotation.



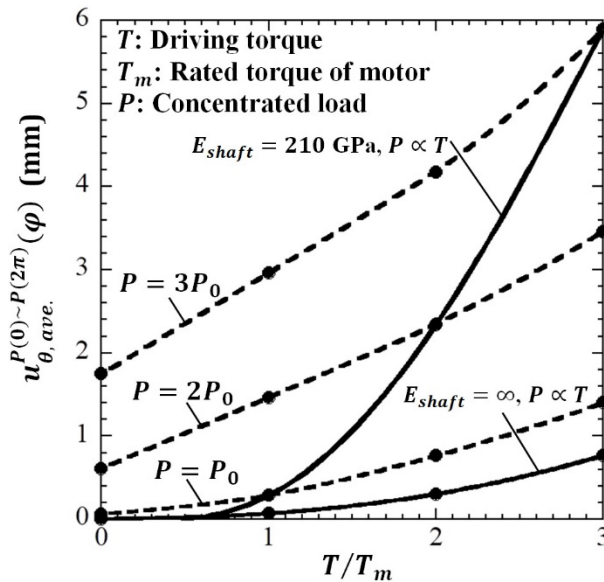
(a) Circumferential interface displacement distribution increases as $u_{\theta, T=T_m}^{P(0)} < u_{\theta, T=T_m}^{P(0) \sim P(2\pi)} < u_{\theta, T=T_m}^{P(0) \sim P(4\pi)}$. (b) Circumferential interface stress distribution remains as $\sigma_{\theta, T=T_m}^{P(0) \sim P(2\pi)}(\theta)$ and $\sigma_{\theta, T=T_m}^{P(0) \sim P(4\pi)}(\theta)$.

Fig. 4 Interface displacement $u_{\theta, T=T_m}^{P(0)}$ in Fig.1(a) due to the initial load $P = P_0$ increases as can be expressed $u_{\theta, T=T_m}^{P(0)} < u_{\theta, T=T_m}^{P(0) \sim P(2\pi)} < u_{\theta, T=T_m}^{P(0) \sim P(4\pi)}$ by shifting the load as $P(0) \sim P(2\pi) \sim P(4\pi)$ but interface stress distributions remains the same as can be expressed $\sigma_{\theta, T=T_m}^{P(0) \sim P(2\pi)}(\theta) \approx \sigma_{\theta, T=T_m}^{P(0) \sim P(4\pi)}(\theta)$.

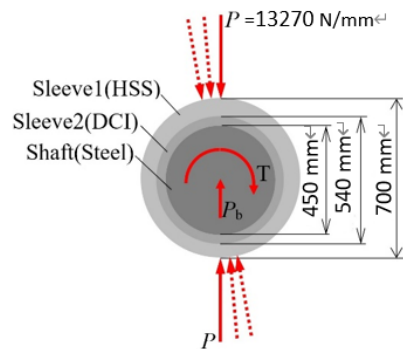
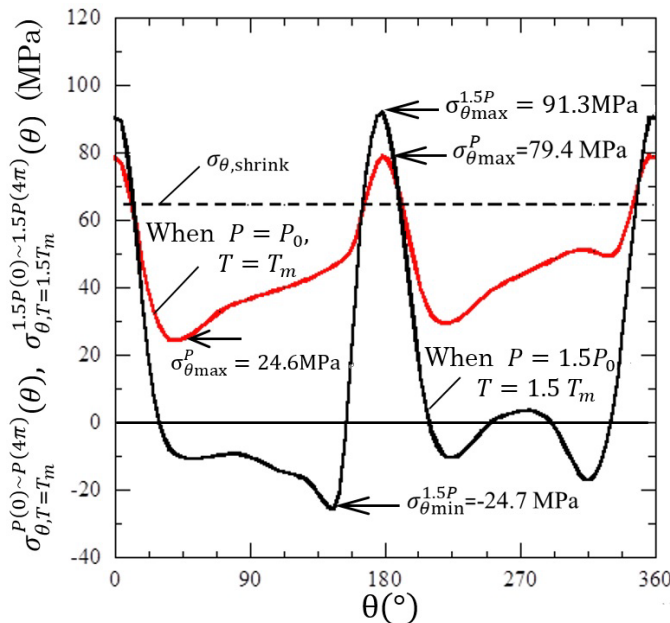
Fig. 5 (a) shows the effect of torque T normalized by the reference value T/T_m on the average displacement $u_{\theta, ave.T}^{P(0) \sim P(2\pi)}(\varphi)$ under one roll rotation $\varphi = 2\pi$ under the standard load $P = P_0$ for the elastic shaft $E_{shaft} = 210$ GPa. The results of a rigid shaft $E_{shaft} = \infty$ is also shown to clarify that the elastic deformation promotes the sleeve slip. With increasing T/T_m , $u_{\theta, ave.T}^{P(0) \sim P(2\pi)}(\varphi)$ increases significantly. The average displacement $u_{\theta, ave.T}^{P(0) \sim P(2\pi)}(\varphi)$ under the rated motor torque $T = T_m$ for the elastic shaft is 4 times larger than that of the rigid shaft, and $u_{\theta, ave.T}^{P(0) \sim P(2\pi)}(\varphi)$ under $T = 3T_m$ for the elastic shaft is 9 times larger than the rigid shaft. As shown in Fig. 6(a), even when $T = 0$, the average displacement $u_{\theta, ave.T}^{P(0) \sim P(2\pi)}(\varphi) \neq 0$, which means under free rolling, the slippage may happen. The detail discussion can be seen in the previous paper [14, 15].

In Fig.5(a), in addition to the no torque condition $T = 0$ and the standard rolling condition $P = P_0, T = T_m$, the extreme condition $P = 3P_0, T = 3T_m$ is considered. Here $P = 3P_0, T = 3T_m$ is assumed to be in the state of severe rolling trouble. In Fig.5(a), the solid line shows the effect of T/T_m on the average displacement $u_{\theta, ave.T}^{P(0) \sim P(2\pi)}(\varphi)$ when both P and T increase proportionally. The average displacement $u_{\theta, ave.T}^{P(0) \sim P(2\pi)}(\varphi)$ for the elastic shaft $E_{shaft} = 210$ GPa under $P = 3P_0, T = 3T_m$ is 20 times larger than that of $P = P_0, T = T_m$. In Fig. 5 (a), the dotted line shows the average displacement $u_{\theta, ave.T}^{P(0) \sim P(2\pi)}(\varphi)$ when the load P is fixed as $P = P_0, P = 2P_0, P = 3P_0$ by varying the motor torque T . Under fixed $P = P_0$, the average displacement $u_{\theta, ave.T}^{P(0) \sim P(2\pi)}(\varphi)$ at $T = 3T_m$ is 5 times larger than $u_{\theta, ave.T}^{P(0) \sim P(2\pi)}(\varphi)$ at $T = T_m$. However, under fixed $T = T_m$, the average displacement $u_{\theta, ave.T}^{P(0) \sim P(2\pi)}(\varphi)$ at $P = 3P_0$ is 10 times larger than that at $P = P_0$. This observation explained that the effect P on the average displacement $u_{\theta, ave.T}^{P(0) \sim P(2\pi)}(\varphi)$ is larger than the effect T .

Fig. 5(b) shows the stress distribution along the interface $\sigma_{\theta,T=T_m}^{P(0)\sim P(4\pi)}(\theta)$ when the load $P = P_0$ moves two rotations as $P(0)\sim P(4\pi)$ in comparison with the stress distribution $\sigma_{\theta,T=1.5T_m}^{1.5P(0)\sim 1.5P(4\pi)}(\theta)$ when the load $P = 1.5P_0$ moves as $P(0)\sim P(4\pi)$. Under the load $P = P_0$, the maximum stress is $\sigma_{\theta,max}^{P_0} = 79.4$ MPa and the minimum stress is $\sigma_{\theta,min}^{P_0} = 24.6$ MPa. On the other hand, under the load $P = 1.5P_0$, which is corresponding to the impact load when the rolled plate biting trouble occurs, the maximum stress is $\sigma_{\theta,max}^{1.5P_0} = 91.3$ MPa and the minimum stress is $\sigma_{\theta,min}^{1.5P_0} = -24.7$ MPa. Here, the stress amplitude σ_a and the mean stress σ_m are expressed in Equations (2) and (3).



(a) Increase of the average displacement $u_{\theta,ave,T=T_m}^{P(0)\sim P(\varphi)}(\varphi)$ with increasing T/T_m when $P = P_0$, $P = 2P_0$ and $P = 3P_0$. It should be noted that if $P \neq 0$ the slip may happen even if $T = 0$.



(b) Circumferential interface stress distribution $\sigma_{\theta,T=T_m}^{P(0)\sim P(4\pi)}(\theta)$ in Fig.2 under standard loading condition $P = P_0$ and $T = T_m$ in comparison with $\sigma_{\theta,T=1.5T_m}^{1.5P(0)\sim 1.5P(4\pi)}(\theta)$ under impact loading condition $P = 1.5P_0$ and $T = 1.5T_m$. Under the impact force $P = 1.5P_0$, the stress amplitude σ_a is about 2.1 times larger than the stress under the standard load $P = P_0$.

Fig. 5 Effect of rolling load P and motor torque T on the slip amount $u_{\theta,ave,T=T_m}^{P(0)\sim P(\varphi)}(\varphi)$ and stress distribution $\sigma_{\theta,T=T_m}^{P(0)\sim P(4\pi)}(\theta)$ at the shrink-fitted interface.

4. Miniature Roll Experiment Proposed to Verify the Simulation Results and to Identify Unknown Slip Defect Geometry

Fig. 6 (a) illustrates the actual roll at the central cross section in Fig. 1(a). Fig.6 (b) shows a miniature roll whose diameter is 60 mm used to verify the sleeve slip experimentally [29, 30]. The miniature roll's diameter is about 1/10 of the real roll. As shown in Fig.6 (b), the miniature roll consists of the sleeve, the outer shaft and the inner shaft. The inner and outer shafts are fixed by key so that the interfacial slippage between the outer shaft and the sleeve shrink-fitted can be prevented. In the miniature roll experiment, the work roll is cooled down by water at room temperature to prevent the change of the shrink-fitting ratio due to rising temperature. Under the steady rotation, the load of 1 ton is applied confirming the roll surface temperature change was within 5°C or less during the experiment by a contact thermometer.

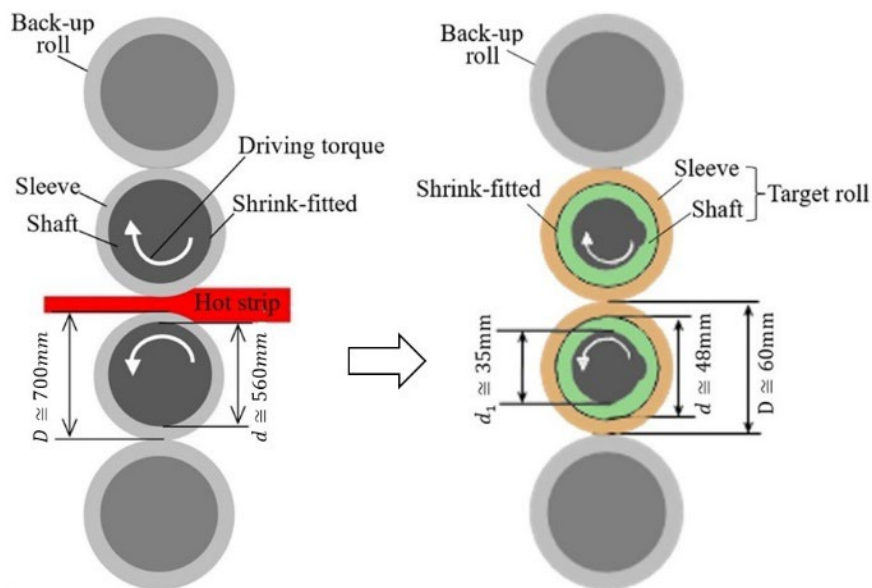
Since a similar phenomenon is known in ball/roller bearing as “interface creep”, the slippage is verified under free rolling. Note that, even when there is no shrink-fitting as $\delta/d = 0$, the sleeve and the shaft managed to be in contact with each other due to the load P in Fig. 6 (b). Hence, the shrink-fitting ratios of $\delta/d = 0$ and $\delta/d = 0.21 \times 10^{-3}$ are considered. When $\delta/d = 0$, the slip angle $\theta_{slip} = 76^\circ$ and the slip distance $\ell_s = \pi d \theta_{slip} / 360 = 31.8$ mm occurs after the number of the roll rotation $n = 1 \times 10^4$. When $\delta/d = 0.21 \times 10^{-3}$, the slip angle $\theta_{slip} = 77^\circ$ and the slip distance $\ell_s = \pi d \theta_{slip} / 360 = 32.3$ mm occurs after the number of the roll rotation $n = 3 \times 10^4$.

The numerical simulation is newly performed for the miniature roll in Fig.6 (b). Similar to the actual roll simulation, since the displacement $u_{\theta}^{P(0) \sim P(\varphi)}(\theta)$ varies depending on θ , the average displacement can be defined in Eq.(2) [11-15, 29-31].

$$u_{\theta,ave}^{P(0) \sim P(\varphi)} = \frac{1}{2\pi} \int_0^{2\pi} u_{\theta}^{P(0) \sim P(\varphi)}(\theta) d\theta \quad (\text{numerical simulation}) \approx \ell_s \quad (\text{experiment}) \quad (2)$$

The simulation results showed the average displacement $u_{\theta,ave}^{P(0) \sim P(\varphi)}$ was initially unstable but became stable from after one rotation [23]. The slip distance per rotation n ℓ_s/n can be expressed as shown in Eq. (2).

$$\ell_s/n \quad (\text{experiment}) = \frac{\theta_{slip} \pi d}{360 \cdot n} \approx u_{\theta,ave}^{P(0) \sim P(2n\pi)} / n \quad (\text{numerical simulation}) \quad (3)$$



(a) Real roll at the central cross section

(b) Miniature roll at the central cross section

Fig. 6 Schematic illustration for (a) Real roll and (b) Miniature roll.

Table 2 Comparison of the experimental results and the simulation results in Fig. 6 (b).

Shrink-fitting ratio δ/d	Displacement increase rate		Relative displacement	
	$\frac{du_{\theta,ave.}^{P(0)\sim P(2n\pi)}}{d\varphi} \approx \frac{\pi d\theta_{slip}}{360^2(n_t - n_0)}$ (mm/deg.)		$u_{\theta,ave.}^{P(0)\sim P(2n\pi)} \approx \ell_s = \frac{\pi d\theta_{slip}}{360(n_t - n_0)}$ (mm/rev.)	
	Experiment (mm/deg.)	Simulation (mm/deg.)	Experiment (mm)	Simulation (mm)
$\delta/d = 0$	0.884×10^{-5}	3.074×10^{-5}	0.318×10^{-2}	1.356×10^{-2}
$\delta/d = 0.21 \times 10^{-3}$	0.299×10^{-5}	1.103×10^{-5}	0.108×10^{-2}	0.384×10^{-2}

Table 2 compares the experimental results and the numerical simulation results regarding the displacement increase rate $du_{\theta,ave.}^{P(0)\sim P(2n\pi)}/d\varphi$ and the slip distance $\ell_s = \frac{\pi d\theta_{slip}}{360} \approx u_{\theta,ave.}^{P(0)\sim P(2n\pi)}$. The simulation results in Table 6 are based on the results where the slip appears at the same time when the roll rotation starts, and consistently appears throughout the roll rotation without causing the slip defect. From Table 2, it is seen that the simulation results are 3.6~4.3 times larger than the experimental results. This difference can be explained from a constant friction coefficient $\mu = 0.3$ assumed in the simulation, even though the friction coefficient is kept changing like $\mu = 0.3\sim\infty$ throughout the experiment due to the growth of the slip defect. In the experimental observation, due to the circumferential slip, slip defects start with thin and shallow scratches, then, it becomes thicker and deeper with erosive wear and cohesive wear, and eventually form large defects that completely stop the slip. In the simulation, the constant friction coefficient $\mu = 0.3$ should be changed to $\mu = 0.3\sim\infty$, but actually the change reflecting the real defect evolution is almost impossible in practice. This is the reason why 3.6~4.3 times difference appears between the experiment and the simulation. Although the results are comparatively larger, the current simulation can still be used for comparative purposes. For example, both experiment and numerical simulation showed that the results under no shrink-fitting of $\delta/d = 0$ is 2.79~3.53 times larger than the results of $\delta/d = 0.21 \times 10^{-3}$.

In the previous study on the actual rolls shown in Fig. 1, the depth of the slip defects was reported, but not their detailed dimensions, which are necessary to evaluate the fatigue strength of the sleeve rolls. In addition, an experimental approach should be conducted to validate the load shifting simulation method. Fig. 7 shows an example of the defect observed on the sleeve surface after slippage. The three-dimensional geometry of the defect was investigated by cutting the specimen long the cross section at the AA' and BB'. Then, it was found that the slip defect can be approximated by an ellipsoid. As can be expressed $(x/a)^2 + (y/b)^2 + (z/c)^2 = 1$, $a = 1000 \mu m$, $b = 250 \mu m$, $c = 4000 \mu m$, the stress concentration can be estimated as $K_t = 1.14$.

The fatigue strength reduction is evaluated by using the parameter \sqrt{area} , which can be defined as the square root of the projected area of the defect onto a plane perpendicular to the maximum principal stress [32]. Then, the miniature roll's defect can be characterized by $\sqrt{area} = \sqrt{(\pi ab)/2} = 627 \mu m$ from the defect geometry $a = 1000 \mu m$, $b = 250 \mu m$.

In the previous study for real large rolls, the defect depth $b' = 1$ mm was reported after slip in the hot rough rolling sleeve roll whose body diameter $D = 1150$ mm although the detail geometry is unknown [5, 6]. As shown in Fig. 1(a), in this study, the real roll diameter $D = 700$ mm is studied, and the depth of the defect can be a bit smaller than $b' = 1$ mm although it can be larger than the defect depth $b = 0.25$ mm of the miniature roll. Assume that the similar shape of the defect in Fig. 7 is formed due to the slippage in the real roll. By assuming double sizes of the defect of the miniature roll, \sqrt{area} dimension in the real roll can be $\sqrt{area} = \sqrt{\pi(2a)(2b)/2} = 627 \times 2 = 1254 \mu m$. Here $a = 1000 \mu m$ and $b = 250 \mu m$ is the defect dimension of the miniature roll.

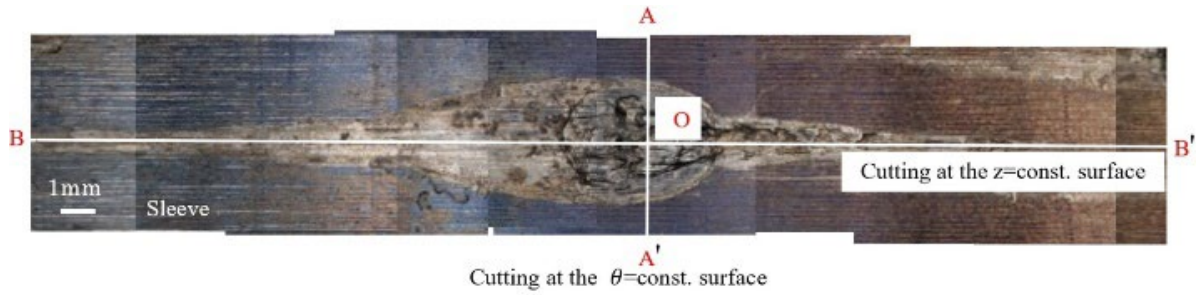


Fig. 7 Example of defect formed by the slippage on the sleeve surface to identify defect dimension observed in the miniature roll in Fig. 6(b) when the shrink fitting ratio $\delta/d = 0.21 \times 10^{-3}$

5. Results and Discussion: Fatigue Strength Evaluation of the Sleeve Roll Using Stress Variation Analyzed and Slip Defect Identified

The fatigue strength of the sleeve roll in Fig.1(a) will be evaluated from the above discussion. The rolling stress $\sigma_{\theta}^{Rolling}$ analyzed in Fig.5 and the defect geometries at the shrink-fitted surface identified in Fig.7 should be utilized. Unlike the commonly used stress amplitude-mean stress diagram (σ_a - σ_m diagram), the σ_a - σ_m diagram of sleeve rolls requires considering the fatigue strength reduction due to slip defects [30]. Regarding the fatigue limit for the engineering material having some defects, Equation (2) was proposed for the stress ratio range $-1 \leq R \leq 0$ [32].

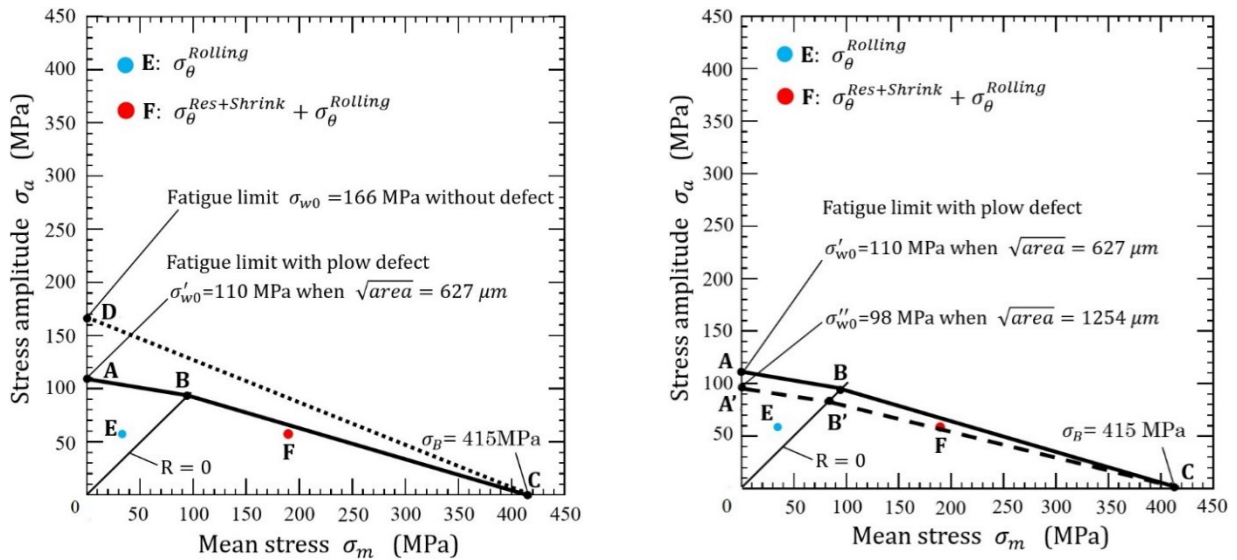
$$\sigma_w = \frac{1.43(H_V+120)}{(\sqrt{area})^{1/6}} \left[\frac{1-R}{2} \right]^{\alpha}, \quad \alpha = 0.226 + H_V \times 10^{-4} \quad \text{when} \quad -1 \leq R = \frac{\sigma_{\theta min}}{\sigma_{\theta max}} \leq 0 \quad (2)$$

where H_V (kgf/mm²) is the Vickers hardness of DCI and $area$ is the projected area of the defect.

Based on the miniature roll experiment, the slip defect size can be characterized by $\sqrt{area} = 627 \mu\text{m}$ [30, 31]. From Equation (2) with $\sqrt{area} = 627 \mu\text{m}$, Fig. 8(a) shows the curve AB as the fatigue limit for the DCI inner layer. Since Equation (2) is proposed based on data in the range $-1 \leq R \leq 0$, the curve AB is indicted for $R = -1 \sim 0$ in Fig. 8(a). Here, Point A corresponds to the fatigue limit of fully reversed loading $R = -1$ of the DCI with the defect size $\sqrt{area} = 627 \mu\text{m}$. Point B can be determined as the intersection of the curve obtained from Equation (2) and the straight line $R = (\sigma_m/\sigma_a - 1)/(\sigma_m/\sigma_a + 1) = -1$. Point B corresponds to the fatigue limit of pulsating tensile load $R = 0$ of the DCI when the defect size $\sqrt{area} = 627 \mu\text{m}$.

In Fig. 8(a), another fatigue limit of the DCI inner layer is provided as the straight-line BC when $\sqrt{area} = 627 \mu\text{m}$. Point C corresponds to the tensile strength of the DCI $\sigma_B = 415 \text{ MPa}$, which must be independent of the slip defect dimension. Recently, Ikeda et al. clarified that the strength of the circumferential notched specimen is larger than the strength of the plain specimen for the wide range of tensile speed and temperature [33]. Therefore, the static strength of DCI including some defects can be the same as the tensile strength of the DCI without defects $\sigma_B = 415 \text{ MPa}$.

In Fig. 8(a), the common fatigue limit line DC for the DCI with no defect is also shown as a dotted line in comparison with the fatigue limit ABC explained above when $\sqrt{area} = 627 \mu\text{m}$. Point D corresponds to the fatigue limit of fully reversed loading $R = -1$ when DCI has no slip defect. Then, the rolling stress $\sigma_{\theta}^{Rolling}$ under the impact force condition $P = 1.5P_0, T = 1.5T_m$ are considered. In Figure 8(a), Point E shows stress amplitude and mean stress (σ_a, σ_m) due to the rolling stress $\sigma_{\theta}^{Rolling}$ and shrink fitting stress σ_{θ}^{Shrink} . Point F shows stress amplitude and mean stress (σ_a, σ_m) due to the rolling stress $\sigma_{\theta}^{Rolling}$, shrink fitting stress σ_{θ}^{Shrink} and residual stresses σ_{θ}^{Res} . Here, the mean stress is obtained by superposing those stresses as $\sigma_{\theta}^{Res+Shrink} + \sigma_{\theta}^{Rolling} = 189.3 \text{ MPa}$.



(a) Fatigue limit diagram for Fig.1 (a) when the slip defect $\sqrt{areaa} = 627 \mu\text{m}$ to evaluate two critical points. The dotted line shows the case of no defect. (b) Fatigue limit diagram for Fig.1 (a) when the slip defect $\sqrt{areaa} = 1254 \mu\text{m}$.

Fig.8 Stress amplitude σ_a vs. mean stress σ_m diagram considering slip defect for $\sigma'_{w0} = 110 \text{ MPa}$ when $\sqrt{areaa} = 627 \mu\text{m}$, $\sigma''_{w0} = 98 \text{ MPa}$ when $\sqrt{areaa} = 1254 \mu\text{m}$ and $\sigma_B = 415 \text{ MPa}$. Point E shows (σ_a, σ_m) due to the rolling and shrink fitting stresses, and Point F shows (σ_a, σ_m) due to the rolling, shrink fitting and residual stresses

In Section 4, as well as the slip defect dimensions in the miniature roll experiment, the slip defect dimensions in the standard sleeve roll in Figure 1(a) was discussed as $\sqrt{areaa} = \sqrt{\pi(2a)(2b)/2} = 627 \times 2 = 1254 \mu\text{m}$. In Fig. 8(b), Point A' corresponds to the fatigue limit of fully reversed loading $R = -1$ with defect size $\sqrt{areaa} = 1254 \mu\text{m}$. Point B' corresponds to the fatigue limit of pulsating tensile load $R = 0$ with defect size $\sqrt{areaa} = 1254 \mu\text{m}$. If the fatigue limit A'B'C is used, Point F is located on the slightly dangerous side.

Previously, the authors also studied the conventional solid roll without shrink fitting structure. In these studies, first, the suitable residual stress due to quenching were analyzed in the numerical simulation [34-36]. Second, and tempering effect on the residual stress was considered based on the creep experimental test as well as numerical simulation [37, 38]. Third, the rolling stress was clarified with/without considering the residual stress based on stress amplitude σ_a vs. mean stress σ_m diagram extended to compressive mean stress region [39-41]. From the comparison of the results between the solid roll and the sleeve roll in Fig. 8, it may be concluded that if slip damage can be prevented in a suitable way such as proving key between the shrink fit surface, the fatigue strength of the sleeve roll is not very smaller compared to the fatigue strength of the solid roll without shrink-fitting.

6. Conclusions

Next generation rolls such as super-cermet rolls used for rolling can be manufactured only through applying sleeve assembly type structures. Toward preventing peculiar problems of sleeve roll, this review paper summarized the author's recent studies regarding circumferential sleeve slip [11-18]. First, the sleeve slip was realized by load shifting method. Second, the validity of the simulation was confirmed by miniature roll experiment. Third, slip defect geometries were identified. Finally, the fatigue strength of the sleeve roll was discussed by clarifying the stress amplitude during roll rotation. Based on this simulation and experiment, the following conclusions can be obtained.

1) Even under free rolling condition without motor torque, the circumferential slippage occurs. Then, it was found that the slippage is caused by the accumulation of irreversible slip during the roll rotation.

- 2) With increasing the motor torque T as well as the loading force as $P \propto T$, the slip amount increases significantly (see Fig. 5(a)). Under the severe load conditions $T=3T_m$ and $P=3P_0$ corresponding to the rolling trouble, the slip amount (= average displacement $u_{\theta,ave.T}^{P(0)\sim P(2\pi)}(\varphi)$ in Fig.5 (a)) is 20 times larger than that under the standard rolling condition $T=T_m$ and $P=P_0$ (see Fig. 5(a)).
- 3) The miniature roll experiment confirmed the validity of the numerical simulation. The simulation results of the slip amount are 3.6~4.3 times larger than the experimental results. This difference can be explained from a constant friction coefficient $\mu = 0.3$ assumed in the simulation, even though the friction coefficient is kept changing like $\mu = 0.3 \sim \infty$ throughout the experiment due to the growth of the slip defect.
- 4) The three-dimensional geometry of the slip defect was identified by cutting the specimen. By using the parameter \sqrt{area} [32], the miniature roll's defect can be characterized by $\sqrt{area} = 627 \mu\text{m}$ from the 3D defect geometry. Here, "area" is the projected area of the defect in the direction to the maximum principal stress.
- 5) The fatigue strength of sleeve assembly rolling rolls can be evaluated by using \sqrt{area} parameter characterizing the identified slip defects. It may be concluded that if there is no large slip damage, the fatigue strength of the sleeve roll is not very smaller compared to the fatigue strength of the solid roll with no shrink-fitting.

References

- [1] H. Shimoda, S. Onodera, K. Hori, Study on the residual deflection of large sleeved back-up rolls: 4th Report, Residual stresses of sleeved rolls. Trans. Jpn. Soc. Mech. Eng. 32 (1966) 689-694.
- [2] T. Irie, K. Takaki, I. Tsutsunaga, Y. Sano, Steel strip and section steel and thick rolling, processing. Tetsu-to-Hagane 65 (1979) 293.
- [3] H. Takigawa, K. Hashimoto, G. Konno, S. Uchida, Development of forged high-speed-steel roll for shaped steel. CAMP-ISIJ 16 (2003) 1150-1153.
- [4] Y. Sano, Recent advances in rolling rolls. Proc of the No. 148-149 Nishiyama Memorial Technology Course, Tokyo, Japan (1993) 193-226.
- [5] Y. Sano, Fatigue failure problem in the inside of roll body for hot strip rolling- Crack initiation problem and its estimation in the actual plant. The 245th JSMS Committee on Fatigue of Materials and the 36th JSMS Committee on Strength Design, Safety Evaluation (1999), 40.
- [6] E. Matsunaga, T. Tsuyuki, Y. Sano, Optimum shrink fitting ratio of sleeve roll (Strength design of shrink fitted sleeve roll for hot strip mill-1). CAMP-ISIJ, 11 (1998) 362. <https://ci.nii.ac.jp/naid/10002551803>.
- [7] S. Tutumi, S. Hara, S. Yoshi, The residual deflection of sleeved backup-up rolls. Tetsu-to-Hagane 57(5) (1971) 818-822.
- [8] S. Spuzic, K.N. Strafford, C. Subramanian, G. Savage, Wear of hot rolling mill rolls: an overview. Wear 176(2) (1994) 261-271. [https://doi.org/10.1016/0043-1648\(94\)90155-4](https://doi.org/10.1016/0043-1648(94)90155-4).
- [9] T. Hattori, Y. Kamitani, K. Sugino, H. Tomita, Y. Sano, Super cermet rolls for manufacturing ultra-fine-grained steel, International Conference on Tribology in Manufacturing Processes ICTMP 2007 International Conference 24-26, Yokohama, September 2007.
- [10] S. Hamayoshi, E. Ogawa, K. Shimiz, N.-A. Noda, Kishi K, S. Koga, Development of large ceramic rolls for continuous hot-dip galvanized steel sheet production lines. Sokeizai 51-12 (2010) 54-59.

-
- [11] N.-A. Noda, D. Suryadi, S. Kumasaki, Y. Sano and Y. Takase, Failure analysis for coming out of shaft from shrink-fitted ceramics sleeve, *Engineering Failure Analysis*, 57 (2015) 219-235.
- [12] G. Zhang, N.-A. Noda, Y. Sano and Y. Takase, Identification of driving out force of shaft towards preventing coming out failure of shaft in shrink-fitted ceramic sleeve roll, *Engineering Failure Analysis*, 135 (2022) 106155.
- [13] N.-A. Noda, H. Sakai, Y. Sano, Y. Takase, Y. Shimoda, Quasi-equilibrium stress zone with residual displacement causing permanent slippage in shrink-fitted sleeve rolls. *Metals* 8 (2018) 998. <https://doi.org/10.3390/met8120998>.
- [14] H. Sakai, N.-A. Noda, Y. Sano, G. Zhang, Y. Takase, Effect of driving torque on the interfacial creep for shrink-fitted bimetallic work roll. *Tetsu-to-Hagane* 105-12 (2019) 28-36. <https://doi.org/10.2355/tetsutohagane.TETSU-2019-048>.
- [15] N.-A. Noda, R.A. Rafar, H. Sakai H, X. Zheng, H. Tsurumaru, Y. Sano, Y. Takase, Irreversible interfacial slip in shrink-fitted bimetallic work roll promoted by roll deformation. *Eng Fail Anal* 126 (2021) 105465. <https://doi.org/10.1016/j.engfailanal.2021.105465>
- [16] N. Soda, *Bearing*. Iwanami Shoten, Tokyo (1964) 196-203.
- [17] Imai: *Lubrication*, 4 (1959) 307.
- [18] J. Murata, T. Onizuka, Generation mechanism of inner ring creep. *Koyo Eng. J.* 166(2005)41-47.
- [19] T. Niwa, A creep mechanism of rolling bearings. *NTN Tech. Rev.* 81 (2013) 100-103.
- [20] Ten, Sakajiri, Takemura, Yukawa: *NSK Tech. J.* 680 (2006) 13.
- [21] *New Bearing Doctor: Diagnosis of bearing problems. Objective: Smooth & reliable operation.* NSK (1997). <https://www.nsk.com/common/data/ctrpPdf/e7005c.pdf>.
- [22] J. Zhan, H. Takemura, K. Yukawa, A study on bearing creep mechanism with FEM simulation. *Proceedings of IMECE2007, 2007 Seattle, Washington, USA.* <https://doi.org/10.1115/IMECE2007-41366>.
- [23] J. Zhan, K. Yukawa, H. Takemura, Analysis of bearing outer ring creep with FEM. *Advanced Tribology*, 2009, Springer, Berlin, Heidelberg. https://doi.org/10.1007/978-3-642-03653-8_74.
- [24] S. Noguchi, K. Ichikawa, A study about creep between inner ring of ball bearing and shaft. *Proceeding of Academic Lectures of the Japan Society for Precision Engineering*, 2010, Japan. <https://doi.org/10.11522/pscjspe.2010A.0.565.0>.
- [25] T. Teramoto, Y. Sato, Prediction method of outer ring creep phenomenon of ball bearing under bearing load. *Trans. Of Society of Automotive Eng. of Japan*, 46 (2015) 355-360. <https://doi.org/10.11351/jsaeronbun.46.355>.
- [26] C. Bovet, L. Zamponi, An approach for predicting the internal behaviour of ball bearings under high moment load. *Mech. Mach. Theory* 101 (2016) 1-22. <https://doi.org/10.1016/j.mechmachtheory.2016.03.002>.
- [27] A. Maiwald, E. Leidich, FE simulations of irreversible relative movements (creeping) in rolling bearing seats –Influential parameters and remedies. *World Congress on Engineering and Computer Science 2013 Vol II*, San Francisco, USA. http://www.iaeng.org/publication/WCECS2013/WCECS2013_pp1030-1035.pdf.
- [28] T. Schiemann, S. Porsch, E. Leidich, B. Sauer, Intermediate layer as measure against rolling bearing creep. *Wind Energy* 21 (2018) 426-440. <https://doi.org/10.1002/we.2170>.

- [29] R.A. Rafar, N.-A. Noda, H. Tsurumaru, Y. Sano Y, Y. Takase, Novel design concept for shrink-fitted bimetallic sleeve roll in hot rolling mill. *Int J Adv Manuf Technol* 120 (2022) 3167-3180. 10.1007/s00170-022-08954-2.
- [30] N.-A. Noda, R.A. Rafar, Y. Taruya, X. Zheng, H. Tsurumaru, Y. Sano, Y. Takase, K. Nakagawa, K. Kondo, Interfacial slip verification and slip defect identification in shrink-fitted bimetallic sleeve roll used in hot rolling mill, *Tribology International*, 175 (2022) 107793. <https://doi.org/10.1016/j.triboint.2022.107793>
- [31] N.-A. Noda, R.A. Rafar, X. Zheng, H. Tsurumaru, Y. Taruya, Y. Sano, Y. Takase, Fatigue strength analysis of bimetallic sleeve roll by simulation of local slip accumulation at shrink-fit interface caused by roll rotation, *Int J Adv Manuf Technol*, 125 (2023) 369–385. <https://doi.org/10.1007/s00170-022-10669-3>
- [32] Y. Murakami, *Metal fatigue: effects of small defects and nonmetallic inclusions*. Elsevier Science, Oxford UK, 2002.
- [33] T. Ikeda T, N.-A. Noda, Y. Sano, Conditions for notch strength to be higher than static tensile strength in high-strength ductile cast iron. *Eng Fract Mech* 206 (2019)75-88.
- [34] N.-A. Noda, K. Hu, Y. Sano, K. Ono, Y. Hosokawa, Residual stress simulation for hot strip bimetallic roll during quenching *Steel Research International*, 87-11 (2016) 1478-1488.
- [35] N.-A. Noda, K. Hu, Yoshikazu Sano and Yusuke Hosokawa, Usefulness of Non-Uniform Heating and Quenching Method for Residual Stress of Bimetallic Roll: FEM Simulation Considering Creep Behavior, *Steel Research International*, 88-3 (2017) 1600165.
- [36] N.-A. Noda, Y. Sano, M. R. Aridi, K. Tsuboi, N. Oda, Residual stress differences between uniform and non-uniform heating treatment of bimetallic roll: Effect of creep behavior on residual stress. *Metals* 8 (2018) 952.
- [37] N.-A. Noda, M. R. Aridi, R. Torigoe, K. Tsuboi, Y. Sano, Reduction of Residual Stress in Bimetallic Work Roll by Tempering, *Journal of Japan Society for Technology of Plasticity*, 61 (2020) 183-189.
- [38] N.-A. Noda, M. R. Aridi, Y. Sano, Tempering effect on residual stress in bimetallic roll, 35 (2021) 2140044.
- [39] M. R. Aridi, N.-A. Noda, Y. Sano, K. Takata, Z. Sun, Y. Takase, Fatigue failure risk evaluation of bimetallic rolls in four-high hot rolling mills, *Fatigue and Fracture of Engineering Materials and Structures*, 45 (2022) 1065-1087.
- [40] M.R. Aridi, N.-A. Noda, Y. Sano, K. Takata and Z. Sun, Fatigue failure analysis for bimetallic work roll in hot strip mills *Steel Research International*, 93 (2022) 2100313.
- [41] M. R. Aridi, R.A. Rafar, N.-A. Noda, Z. Sun, Y. Sano, K. Takata and Y. Takase, Residual stress simulation for bimetallic sleeve roll constructed by shrink-fitting in comparison with bimetallic solid roll, *Journal of Manufacturing Processes*, 107 (2023) 252-267.